Radio Frequency Tomography for Non-Destructive Testing of Pillars

Tadahiro Negishi, *Student Member, IEEE,* Gianluca Gennarelli, Francesco Soldovieri, *Senior Member, IEEE,* Yangqing Liu, *Student Member, IEEE,* and Danilo Erricolo, *Fellow, IEEE*

***Abstract*—Pillars represent some of the commonest supporting elements of modern and historical buildings. Non-destructive testing methods can be applied to gain information about the status of these structural elements. Among them, ground penetrating radar (GPR) is a popular diagnostic tool for the assessment of concrete structures. Despite several theoretical and experimental studies on concrete structural evaluation by GPR have been reported, little work has been done so far in relation to pillars. Owing to their circular geometry, pillars are complex multi-scattering environments, which render the interpretation of the radar images very challenging. This paper deals with the application of radio frequency tomography as a non-destructive technique for imaging the inner structure of pillars. The main goal of the study is the assessment of the imaging performance that can be obtained in comparison to conventional ground penetrating radar exploiting a multi-monostatic configuration. Accordingly, potentialities and performance of multimonostatic and multiview/multistatic measurement configurations are herein investigated in the inverse scattering framework. For each measurement configuration, the regularized reconstruction of a point-like target and the spectral content are evaluated. The data inversion is carried out by means of the Truncated Singular Value Decomposition scheme. Tomographic reconstructions based on full-wave synthetic data are shown to support the comparative analysis.**

***Index Terms*—Linear inverse scattering, ground penetrating radar, non-destructive testing, radio-frequency tomography.**

I. Introduction

CONCRETE structures unavoidably deteriorate with age and long term exposure to weather conditions. Depending on the type of structure under investigation, different types of damages can arise such as erosion, delaminations, cracks, reinforcement corrosion [1]. These phenomena need to be readily identified and monitored as they can worsen over time and, if neglected, may lead to catastrophic events (e.g. see [2]).

Non-destructive testing (NDT) methods of concrete structures are frequently encountered in civil engineering applications [3], [4]. Most of them exploit acoustic waves at different frequency ranges. A different approach is the electrical resistivity tomography, which relates the electrical conductivity of the structure under test to the metallic phases (reinforcing bars and fibers), cracks and air voids, moisture gradients, and the chloride distribution in the matrix [5], [6]. Another popular tool is Ground Penetrating Radar (GPR) that allows imaging the interior of the structure [7] as a result of the interaction of electromagnetic waves with the hidden anomalies and after a suitable data processing.

In recent years, GPR has been proposed for the assessment of concrete structures such as bridges [8], [9], retaining walls [10], concrete floors [11], dams [12], rebar detection [13], detection of chlorides and moisture in concrete [14]. In all those cases, the radar device collects data along a planar concrete structure. Circular pillars are common supporting elements of buildings, but their structural assessment via GPR has received a little attention, and to the best of the author"s knowledge, relatively few works have been reported [15]–[17]. With the exception of [15], these works are mostly focused on the inspection of columns in historical buildings. Owing to their circular geometry, columns represent a challenging scenario for GPR because complex multipath phenomena (artifact) arise within the structure. These usually produce false targets in the images complicating the interpretation of the scene.

This paper investigates the application of RF tomography (RFT) for the NDT evaluation of pillars, when a multi-view/multistatic measurement configuration is exploited. RFT has been formerly applied to the underground imaging and tunnel detection [18], [19] and has been experimentally validated in [20], [21]. More recently, RFT has been proposed for the imaging of circular pillars and preliminary results were shown in [22], [23]. In this article, a comprehensive analysis of the imaging problem is carried out in a linear inverse scattering framework. More specifically, a study of the imaging performance of RFT configuration is accomplished and a comparative analysis with a conventional GPR configuration, based on multi-monostatic data, is carried out following the idea in [24]. Unlike previous works, an accurate forward model accounting for the presence of the circular air-pillar interface is developed. Moreover, imaging performance are assessed in terms of regularized reconstruction of a point-like target and spectral contents of the relevant operator involved in the linear inverse problem under investigation. A set of tomographic reconstructions based on a numerical model of a concrete pillar is reported to demonstrate the effectiveness of the RFT approach. The linear inverse scattering by an inhomogenous cylinder was addressed in [25]. However, the present study addresses a similar problem under more realistic conditions: incident field generated by filamentary electric currents, observation domain in the near zone, single frequency and multifrequency operation, and 2D image reconstruction.

T. Negishi, Y. Liu and D. Erricolo are with the Department of Electrical and Computer Engineering, University of Illinois at Chicago, Chicago, IL 60607, USA.

G. Gennarelli and F. Soldovieri are with Institute for Electromagnetic Sensing of the Environment, National Research Council of Italy, Via Diocleziano 328, 80124, Napoli, Italy.

Manuscript received XXX, 20XX; revised XXX, 20XX.

The paper is organized as follows. Section II is concerned with the mathematical formulation of the imaging approaches. In Sec. III, the resolution analysis is performed, while tomographic reconstructions based on full-wave data are shown in Sec. IV. Conclusions follow in Sec. V.

II. Problem Statement and Imaging Approach

Let us consider the 2D geometry illustrated in Fig. 1, featuring a dielectric pillar with radius a and characterized by the relative dielectric permittivity ε_b. The medium is assumed to be non-magnetic and lossless, and is probed by transmitting (Tx) and receiving (Rx) antennas deployed along the circumference Γ with radius $\rho_s > a$. Let $\mathbf{r_s} = \rho_s \cos(\phi_s)\hat{x} + \rho_s \sin(\phi_s)\hat{y}$ be the location of the Tx antenna and $\mathbf{r_o} = \rho_s \cos(\phi_o)\hat{x} + \rho_s \sin(\phi_o)\hat{y}$ the position of the Rx antenna. The antennas are modeled as filamentary current lines polarized along the z axis ($\mathrm{TM^z}$ polarization). The investigation domain D contains targets whose presence is described by the contrast function

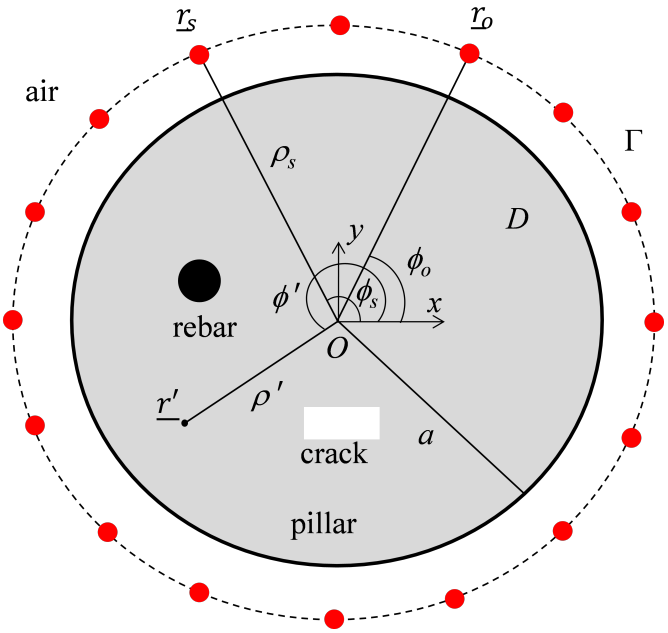

Fig. 1: Geometry of the imaging problem. A pillar with radius a is probed by Tx and Rx antennas deployed along a circumference Γ with radius ρ_s. The structure under test contains reinforcement elements (black circle) or anomalies such as cracks (white rectangle).

$$\chi(\mathbf{r}') = \frac{\varepsilon_t(\mathbf{r}') - \varepsilon_b\varepsilon_0}{\varepsilon_b\varepsilon_0} - j\frac{\sigma_t(\mathbf{r}')}{\omega\varepsilon_b\varepsilon_0}, \tag{1}$$

where $\omega = 2\pi f$ is the angular frequency, ε_0 is the free-space permittivity, ε_t and σ_t are the real permittivity and conductivity functions at any point $\mathbf{r}' = \rho' \cos(\phi')\hat{x} + \rho' \sin(\phi')\hat{y}$ in D, respectively.

During the system's operation, the Tx antennas illuminate the scene by radiating an electromagnetic wave into the pillar and the Rx antennas detect the field scattered by the targets in D. Depending on the locations of the antennas and on the possibility to collect wideband data, the following configurations will be examined:

- Configuration 1 or GPR: multimonostatic/multifrequency configuration ($\phi_o = \phi_s$) operating in the frequency interval $B = (f_{min}, f_{max})$, with f_{min} and f_{max} being the minimum and maximum working frequencies;
- Configuration 2 or single frequency RFT: multiview/multistatic configuration ($\phi_o \neq \phi_s$) operating at the maximum frequency f_{max};
- Configuration 3 or multifrequency RFT: multiview/multistatic/multifrequency configuration ($\phi_o \neq \phi_s$) operating in the frequency range $B = (f_{min}, f_{max})$.

The mathematical formulation of the forward scattering model that will be shown in the following is general and can be specialized to each of the three previous cases by accounting for the proper Tx and Rx angular coordinates and system bandwidth.

Under the Distorted Born approximation [26]–[29], a scalar integral relationship is established between the unknown contrast function χ and the scattered field E_s, i.e.

$$E_s(\mathbf{r_o}, \mathbf{r_s}) = k_b^2 \iint_D g(\mathbf{r_o}, \mathbf{r}')\chi(\mathbf{r}')E_i(\mathbf{r}', \mathbf{r_s})d\mathbf{r}' = \mathcal{L}\chi \tag{2}$$

where k_b^2 is the propagation constant in the medium, E_i is the incident field (i.e. the field in free space) at $\mathbf{r}'$ when the Tx antenna is located at $\mathbf{r_s}$, and g is the scalar inhomogeneous Green's function accounting for the radiation from a point $\mathbf{r}'$in D to the point $\mathbf{r_o}$ in air. The linear integral relationship (2) can be stated as a linear operator $\mathcal{L} : \chi \in X \rightarrow E_s \in Y$, where X denotes the set within which the solution (contrast function) is sought and Y is the set where the data belong to. In particular, we assume X and Y are Hilbert spaces $L^2(D)$ and $L^2(S)$, respectively equipped with the L^2 scalar products $< \cdot, \cdot >_X$ and $< \cdot, \cdot >_Y$. Note that S assumes different expressions according to the three configurations: $S = \Gamma \times B$ for configuration 1, $S = \Gamma \times \Gamma$ for configuration 2 and $S = \Gamma \times \Gamma \times B$ for configuration 3. Moreover, $\mathcal{L}$ is a linear operator mapping the unknown space into data space [28].

By expressing the position vectors in polar coordinates, eq. (2) is rewritten as

$$E_s(\rho_s, \phi_o, \phi_s) = k_b^2 \iint g(\rho_s, \phi_o; \rho', \phi') \times E_i(\rho', \phi'; \rho_s, \phi_s)\chi(\rho', \phi')\rho' d\rho' d\phi'. \tag{3}$$

The incident electric field E_i in D is evaluated by solving the scattering problem involving a dielectric cylinder illuminated by an electrical line source [30]. In detail, by applying cylindrical wave transformations and electromagnetic boundary conditions at the air-pillar interface ($\rho' = a$), one obtains

$$E_i(\rho', \phi'; \rho_s, \phi_s) = -\frac{k_b^2 I_e}{4\omega\varepsilon_b\varepsilon_0} \sum_{n=-\infty}^{\infty} b_n J_n(k_b\rho') e^{jn(\phi' - \phi_s)} \tag{4}$$

where I_e is the complex current at the Tx antenna, J_n is the Bessel's function of first kind and n-th order, and the coefficients b_n are given by

$$b_n = \frac{-2jH_n^{(2)}(\beta_0\rho_s)/(\pi\beta_0 a)}{\mu_r J_n(\beta_1 a) H_n^{(2)\prime}(\beta_0 a) - \sqrt{\varepsilon_r\mu_r} H_n^{(2)}(\beta_0 a) J_n'(\beta_1 a)}. \tag{5}$$

In eq. (5), $H_n^{(2)}$ and $H_n^{(2)\prime}$ are the Hankel's function of second kind and n-th order and its first derivative, respectively.

The inhomogeneous Green's function involved in eq. (3) is evaluated using the reciprocity principle [30], i.e.

$$g(\rho,\phi;\rho',\phi') = -\frac{1}{j\omega\mu_0 I_e} E_i(\rho,\phi;\rho',\phi'). \tag{6}$$

with μ_0 being the magnetic permeability in free space.

According to eq. (3), a linear inverse problem is established and the goal is to determine the unknown contrast function χ from the knowledge of the measured scattered field E_s. Such an inverse problem is ill-posed and a regularization scheme must be applied to achieve a stable solution [28]. According to the definition of the operator $\mathcal{L}$, the reconstruction of the contrast function χ from the knowledge of the scattered field E_s can be stated as the inversion of the operator $\mathcal{L}$. Since $\mathcal{L}$ is a compact operator [28], its Singular Value Decomposition (SVD) can be defined as follows

$$E_s = \mathcal{L}\chi = \sum_{n=1}^{\infty} \sigma_n < \chi, u_n >_X v_n \tag{7}$$

where $\{\sigma_n, u_n, v_n\}_{n=1}^{\infty}$ is the singular spectrum of the operator $\mathcal{L}$ and σ_n is the set of singular values ordered in a not increasing way, while u_n and v_n are the singular functions in the unknown and data space, respectively. In particular, $\{u_n\}_{n=1}^{\infty}$ is an orthonormal basis in the space of the visible objects. The set $\{v_n\}_{n=1}^{\infty}$ forms an orthonormal basis for the subspace of the exact data. Accordingly, the solution of eq. (3) can be stated formally as

$$\chi = \sum_{n=1}^{\infty} \frac{1}{\sigma_n} < E_s, v_n >_Y u_n \tag{8}$$

A proper way to regularize the inverse problem, exploited in the present paper, is the Truncated Singular Value Decomposition scheme, where the approximate (regularized solution) is achieved by means of the inversion formula

$$\hat{\chi} = \sum_{n=1}^{N_t} \frac{1}{\sigma_n} < E_s, v_n >_Y u_n \tag{9}$$

where N_t acts as the regularization parameter and is a truncation index selected as trade-off between achieving a physical meaningful and a stable solution.

The spatial map defined by the modulus of the retrieved contrast function $\hat{\chi}$ is the output of the inversion algorithm. The space region where the retrieved contrast function is significantly different from zero accounts for the presence and location of the targets.

III. Imaging performance of the measurement configurations

This Section deals with the analysis to assess the imaging performance of the three measurement configurations defined in Sec. II. The analysis is carried out by two different figures of merit as follows.

The first one is the regularized reconstruction of a point-like target [28], which is carried out according to the steps of the approach described in [31], which is briefly summarized for clarity of the explanation. First, model data for the point target are generated and corrupted by Additive White Gaussian Noise (AWGN) to account for the effect of noise. Then, the L-curve method [32], [33] is applied to find the optimal regularization parameter of the TSVD inverse scheme, which is expressed as the number of retained terms N_t. This regularization parameter accounts for the trade-off to minimize both the norm of the solution $||\chi||_2$ and the norm of the residue $||E_s - \mathcal{L}\chi||_2$.

After that the regularization parameter N_t has been determined, we introduce the second figure of merit, i.e., the the spectral content of the scattering operator $\mathcal{L}$. The spectral content concept has been applied in the past to study different radar imaging problems (e.g. see [34]–[38]). The spectral content accounts for the retrievable spatial harmonics of the unknown contrast function following the adopted regularized inversion scheme. As it will be shown, differently from the regularized reconstruction of the point target, the spectral content provides global information related to the considered investigation domain rather than information at a specific location inside the investigation domain. This is made clear by the following derivation.

Let us consider the regularized point-spread-function (PSF) related to a point target at $\mathbf{r_o}$ and expressed in terms of the SVD, i.e.

$$\mathrm{PSF}(\mathbf{r}', \mathbf{r_o}) = \sum_{n=1}^{N_t} v_n(\mathbf{r}') v_n^*(\mathbf{r_o}) \tag{10}$$

and compute its Fourier transform with respect to the spatial variables x' and y'

$$\widehat{\mathrm{PSF}}(\mathbf{k}, \mathbf{r_o}) = \sum_{n=1}^{N_t} \hat{v}_n(\mathbf{k}) v_n^*(\mathbf{r_o}) \tag{11}$$

with $\mathbf{k} = k_x\hat{x} + k_y\hat{y}$ (k_x and k_y are the conjugated spectral variables corresponding to x' and y'), and

$$\hat{v}_n(\mathbf{k}) = \iint_D v_n(\mathbf{r}') \exp(-j\mathbf{k}\cdot\mathbf{r}') d\mathbf{r}' \tag{12}$$

Then, we evaluate the square amplitude of both sides of eq. (11), thus getting

$$|\widehat{\mathrm{PSF}}(\mathbf{k}, \mathbf{r_o})|^2 = \left(\sum_{n=1}^{N_t} \hat{v}_n(\mathbf{k}) v_n^*(\mathbf{r_o})\right)\left(\sum_{m=1}^{N_t} \hat{v}_m^*(\mathbf{k}) v_m(\mathbf{r_o})\right) \tag{13}$$

As the spectral functions involved in eq. (13) depend on the specific target position $\mathbf{r_o}$, we integrate over all possible posi-

tions in order to obtain global (average) spectral information SC defined as

$$\mathrm{SC}(\mathbf{k}) \triangleq \iint_D |\widehat{\mathrm{PSF}}(\mathbf{k},\mathbf{r_o})|^2 d\mathbf{r_o} = \sum_{n=1}^{N_t}\sum_{m=1}^{N_t} \hat{v}_n(\mathbf{k})\hat{v}_m^*(\mathbf{k}) \iint_D v_n^*(\mathbf{r_o}) v_m(\mathbf{r_o}) d\mathbf{r_o} \qquad (14)$$

In view of the orthonormality of the singular functions v_n and v_m, the spectral content reduces as

$$\mathrm{SC}(\mathbf{k}) = \sum_{n=1}^{N_t} |\hat{v_n}(\mathbf{k})|^2. \qquad (15)$$

Before showing the numerical tests, it is worth noting that the PSF definition in eq. (9) is only exploited to derive the spectral content and is not used to compare the resolution performance of the three imaging configurations at hand. Indeed, the computation of the PSF via eq. (11) would enable only a comparison for the same value of the truncation index N_t, which ultimately depends on the noise on data. Here, we adopt the approach described in [31] to enable a fair comparison for the same value of the signal-to-noise-ratio (SNR) on the data.

The numerical test refers to a pillar characterized by a dielectric constant $\varepsilon_b = 4$ and a radius $a = 0.2$ m. Fifty Tx and Rx antennas collect data along a circumference of radius $\rho = 0.21$ m. The investigation domain D coincides with the pillar and is discretized into square pixels having size 0.01 m.

The reason for choosing this number of transmitters and receivers is to ensure data redundancy, so that the discretized versions (matrices) of the operators are good approximations of the "continuous" operators. Indeed, the singular values curve spans more than 100 dB below the maximum singular value; this means that we are able to capture all the information about the scattered field with this number of transmitters and receivers. The evaluation of the incident field is carried out via eq. (4), where Shanks transform [39] is used to accelerate the convergence rate of the series and 45 terms are used at the most.

The performance analysis is carried out for a point target located at $(0.1, 0.1)$ m as seen in Fig. 2. The scattered field data are computed over the frequency range (1000, 2950) MHz with a step of 150 MHz. In order to have fair comparisons for all 3 configurations, we corrupt the data by AWGN so that a SNR = $(30, 10, -10)$ dB is achieved for configuration 3. For the other two configurations, we have downsampled the corrupted data from configuration 3.

The curves plotted in Fig. 3 display the singular values of the operator $\mathcal{L}$ for the three measurement configurations. As can be seen, aside from the initial decay, all the curves exhibit a similar behavior that is almost flat before the exponential decay, which takes place after their knee. Such a knee occurs at a lower index in configuration 1 (GPR) compared to configuration 2 (single frequency RFT) and configuration 3 (multifrequency RFT). This suggests that (1) fewer singular values are generally available to reconstruct the contrast function in configuration 1 resulting in a worse imaging performance; (2) a similar number of singular values is expected in configurations 2 and 3 with comparable performance in terms of spatial resolution. Table I summarizes the values of the choice of the regularization parameters N_t for the three configurations and different values of the SNR = $(30, 10, -10)$ dB. N_t is estimated by using the L-curve method. As long as the SNR increases, the number of singular values also increases. In addition, for a fixed SNR, we observe an increase of the number of singular values when we turn from the monostatic (GPR) configuration to the multi-view/multi-static (RFT) configurations. Note that configurations 2 and 3 are characterized by the same number of singular values for the three SNR levels.

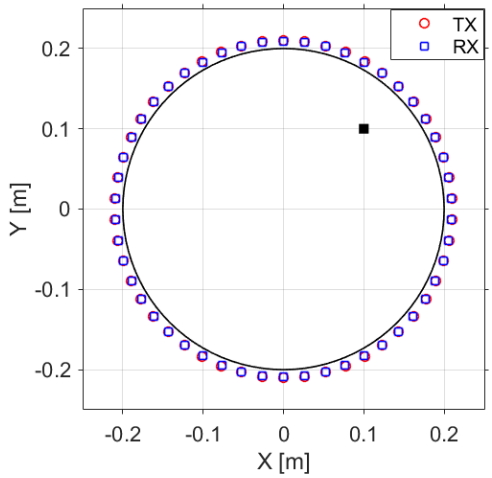

Fig. 2: Geometrical arrangement of Tx and Rx around the pillar. The black square denotes a point-like target.

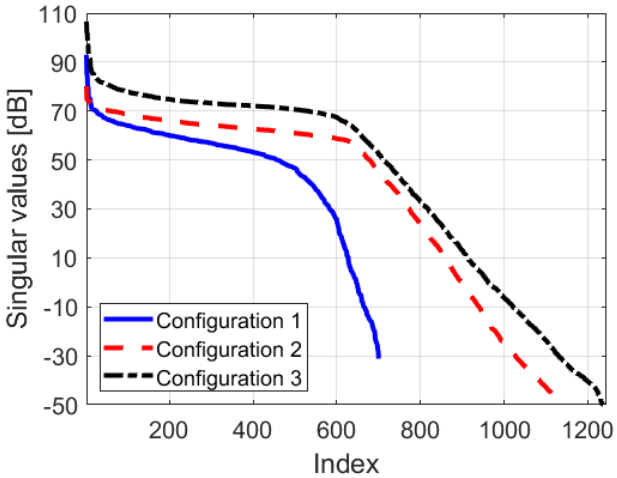

Fig. 3: Singular values of the operator $\mathcal{L}$ for each measurement configuration.

The images plotted in Fig. 4 depict the normalized amplitude of the regularized reconstructions for the considered configurations and SNR values. The top row refers to SNR = 30 dB and highlights that the target is correctly reconstructed in each case and it is only slightly better resolved with configurations 2 and 3. When the data noise level increases,

TABLE I: Optimal truncation index N_t vs. measurement configuration and SNR

SNR [dB]	Configuration 1	Configuration 2	Configuration 3
-10	498	657	657
10	531	708	708
30	600	768	768

TABLE II: Entropy of the regularized reconstruction of the point-like target

SNR [dB]	Configuration 1	Configuration 2	Configuration 3
-10	6.58	6.48	5.23
10	5.11	3.49	2.56
30	3.40	2.29	2.21

SNR = +10 dB (middle row), the GPR configuration still allows identifying the target but the image quality degrades compared to the RFT configurations in terms of both resolution and artifacts. When the data are very noisy, SNR = -10 dB (bottom row), the GPR configuration fails to image the target since the reconstruction is totally corrupted by the noise. When we turn to both RFT configurations, we observe that the reconstruction of the point target allows to achieve similar resolutions limits; in addition, the multi-frequency RFT image looks slightly cleaner and this is confirmed also by the analysis below regarding the "entropy" indicator (see Table II). The lower noise in the multifrequency RFT image can be explained by considering that, due to the linearity of the model and additivity of noise, the reconstructed PSF at a point $\mathbf{r_o}$ can be written as

$$\mathrm{PSF}(\mathbf{r}', \mathbf{r_o}) = \sum_{m=1}^{N_t} v_m(\mathbf{r}') v_m^*(\mathbf{r_o}) + \sum_{m=1}^{N_t} \frac{< \mathbf{n}, u_m >}{\sigma_m} v_m(\mathbf{r}') \tag{16}$$

where the first summation is the noise-free PSF reconstruction (see eq. (10)) and the second summation is the noise contribution to the reconstruction. Since the singular values are larger in the multifrequency RFT configuration (see Fig. 3), it can be argued that the noise contribution to the reconstruction is smaller compared to the one achieved by single frequency RFT.

In order to provide a quantitative criterion to assess the image quality, the entropy E of each image is evaluated according to the formula [31]

$$E = -\sum_{p=1}^{P_t} ss(x_p, y_p) \ln[ss(x_p, y_p)] \tag{17}$$

where

$$ss(x_p, y_p) = |\chi(x_p, y_p)|^2 / \sum_{q=1}^{P_t} |\chi(x_q, y_q)|^2. \tag{18}$$

is the normalized square amplitude of the contrast function at the point (x_p, y_p) and P_t is the number of pixels in the image. We recall that the entropy in eq. (17) measures the contrast of an image and assumes higher values when the image has a poor resolution and/or large presence of artifacts.

The entropy values of the regularized reconstruction of the point-like target in Fig. 4 are summarized in Tab.II. The data point out that, regardless of noise level, multifrequency RFT generally provides better resolved images, with reduced presence of artifacts, compared to single frequency RFT and GPR. In addition, the two RFT configurations have similar performance for the cases of SNR = 10 and 30 dB; there is only a small difference for the case of SNR = -10 dB.

In the following, the spatial spectral coverage of the scattering operator $\mathcal{L}$ is examined where the regularization parameter is chosen according to the L-curve analysis (see Tab. I).

The spectral contents corresponding to SNR = $(30, 10, -10)$ dB are computed for each configuration. Note that due to the symmetry of the scenario and of the measurement domain, the spectral contents have a rotational symmetry. For this reason, the spectral content is depicted in Fig. 5 along a radial cut in the spectral domain. For each configuration, the theoretical spectral content predicted by diffraction tomography [40], [41] in the case of a homogeneous medium is represented for comparison purposes (see colored regions between the vertical black lines). In the GPR configuration, such a set is the annular ring delimited by the circumferences having radii $2k_{b,min}$ and $2k_{b,max}$, with $k_{b,min}$ and $k_{b,max}$ being the propagation constants of the medium at the minimum and maximum frequency, respectively [34]. In the single frequency and the multifrequency RFT, the theoretical spectral coverage is the Ewald's circle with radius $2k_{b,max}$ [41]. Therefore, for the same maximum frequency, single frequency and multifrequency RFT have the same theoretical spectral coverage and hence a similar resolving power. This claim is also valid for the case of an inhomogeneous background medium as confirmed by the spectral contents in Fig. 5 (configurations 2 and 3) and supported by the regularized reconstruction of the regularized reconstruction of the point target in Fig. 4.

For the GPR configuration, the inhomogeneous model described by eqns. (4) - (6) introduces a major difference in the spectral content. While the theoretical spectral content for a homogeneous model has a spectral hole with radius $2k_{b,min}$, the linear scattering operator for inhomogeneous model tends to fill all the Ewald's circle. In fact, the low frequency spectrum components now can be partially recovered thanks to the multiscattering effect arising within the pillar. These multiscattering effects are pictorially depicted in Fig. 6, and show how an increase the illumination/observation diversity for GPR configuration is achieved due to the reflection phenomena at the pillar/air interface.

A similar phenomenon has been recently observed in relation to the radar imaging through periodic structures [36], [37] and in urban canyons [42], [43].

We recall that the spectral content is a measure of the resolving power for targets located anywhere in the investigation domain. In this sense, Fig. 5 reveals that all configurations have similar imaging performance. However, the spectral content does not provide information about the detectability of the targets, which can be inferred instead from the point target analysis of Fig. 4.

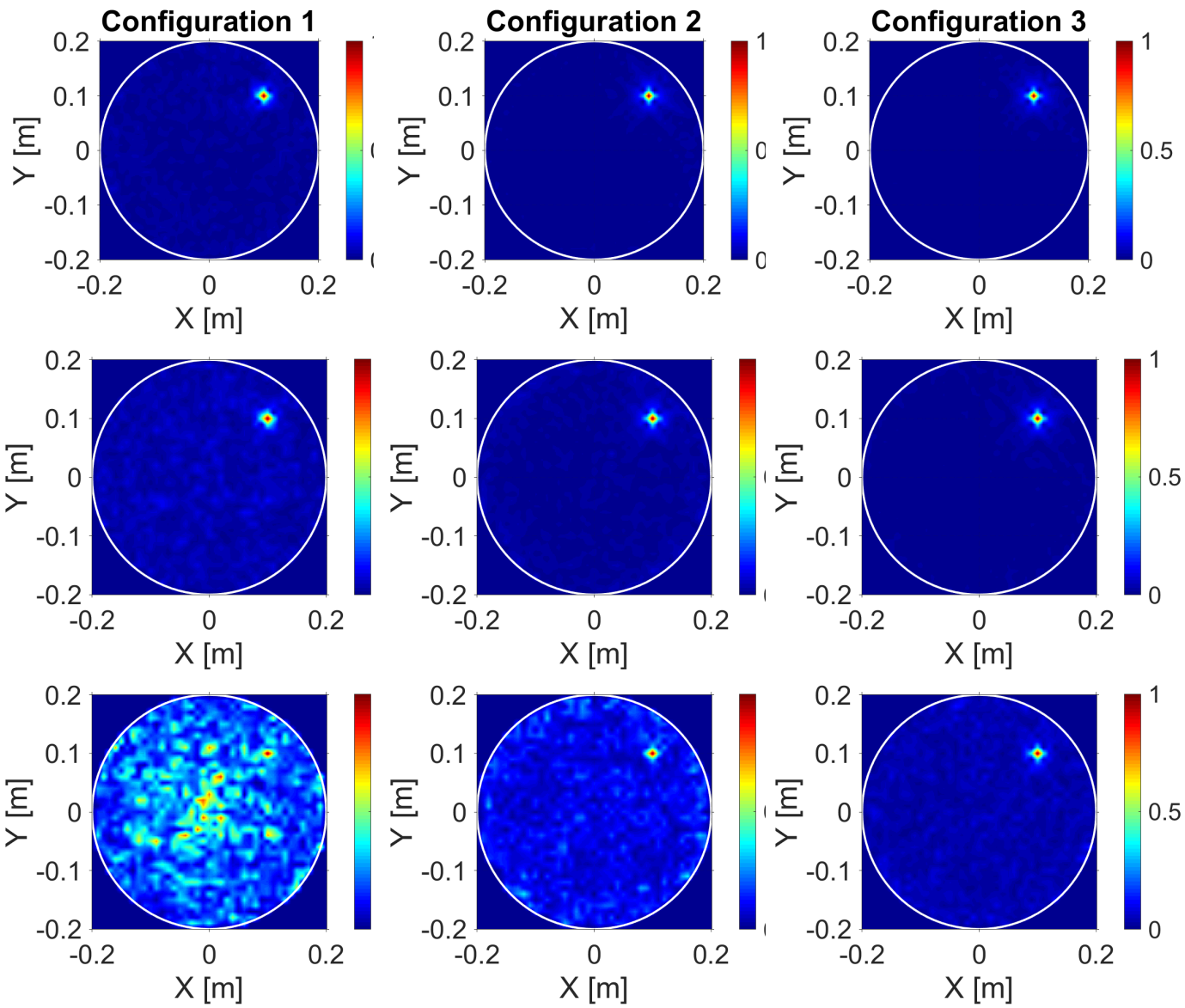

Fig. 4: Normalized amplitude (given by eq. (7)) of the regularized reconstruction of a point-like target located at [0.1, 0.1] m for each measurement configuration and SNR level, according to SNR = +30 dB (top row), SNR = +10 dB (middle row), and SNR = -10 dB (bottom row).

IV. Reconstruction results

In this Section, tomographic reconstructions are provided by processing full-wave synthetic data generated by the commercial software FEKO [44] based on the Method of Moments [45]. The numerical tests refer to the dielectric pillar, measurement configurations, and data processing parameters considered in Sec. III. Moreover, for data generation, the pillar is also assumed to be lossy and characterized by the electrical conductivity 0.005 S/m. 2D full-wave simulations are carried out in the xy plane by using wire sources as Tx antennas and setting periodic boundary conditions along z. The scattered field data are obtained by means of a background subtraction, i.e. computing the difference between the total field in presence of targets and the field recorded in the case of an empty pillar. After, the scattered field data are corrupted with AWGN for SNR = $(+30, +10, -10)$ dB as done according to the procedure described in Sec. III. The regularization parameter has been determined according to the L-curve method and used in the reconstruction.

A comprehensive set of test cases featuring pillars containing different types of targets is considered as listed below:

- 1 metallic and 1 void cylinder (A);
- 2 metallic cylinders and 1 metallic rectangular bar (B);
- 1 metallic cylinder with a nearby crack (C).

Three scenarios described above are represented in Figs. 7, 8, 9 and together with the corresponding tomographic reconstructions related to each measurement configuration and SNR level. In all the tests, the cylinders have radius 0.025 m and are centered at (0.1, 0.1) m and (-0.1, -0.1) m.

The images in Fig. 7 deal with the most favorable situation

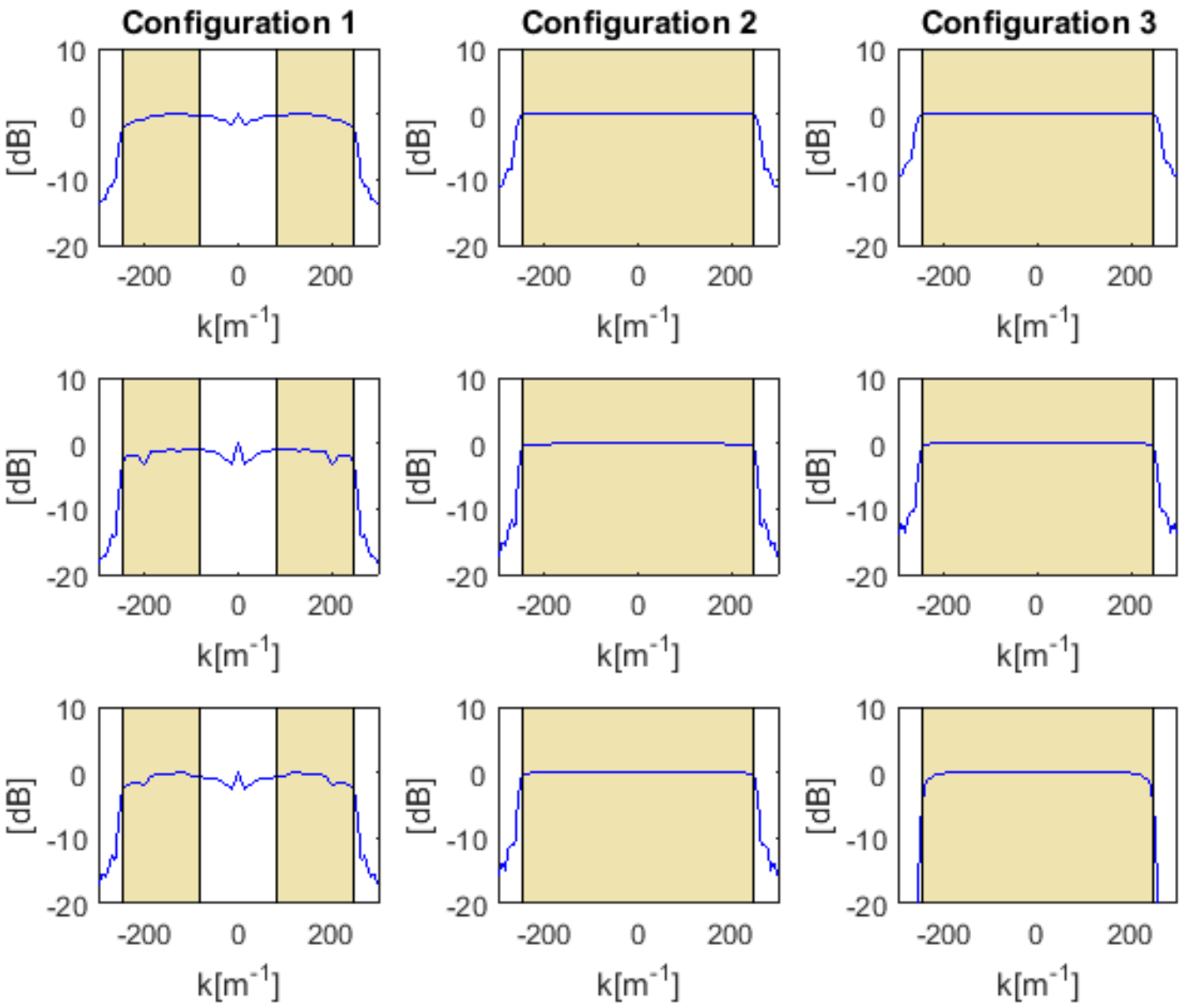

Fig. 5: Radial cut of the spectral contents. First row SNR=30 dB; second row SNR= 10 dB; third row SNR=-10 dB. Left column: Configuration 1; middle column: Configuration 2; right column: Configuration 3. The theoretical spectral sets are the colored regions between the vertical black lines.

in terms of noise level (SNR = +30 dB). As can be seen, the GPR configuration (Fig. 7(b)) is not very reliable since the reconstructions contain many artifacts and, in some cases, the targets are not easily detectable (see void cylinder in scenario A and all targets in scenario B). The images achieved with single frequency RFT (Fig. 7(c)) highlight a lower presence of artifacts and the contours of the targets are slightly better defined. Notably, metallic cylinders are clearly distinguished from void cylinders because only the contour is imaged due to their non-penetrating characteristic. The scenario B still remains a challenging situation for single frequency RFT, where only the target in the center is partially reconstructed and the two metallic cylinders appear as strong as artifacts, due to the relatively low distance among the targets. The reconstruction achieved in the case of the metallic cylinder with a crack (scenario C) confirms that crack detection is more reliable with single frequency RFT with respect to GPR. The reconstructions provided by the inversion of multifrequency RFT data (Fig. 7(d)) have a superior quality in all test cases. Specifically, the contours of the targets are very well defined even in the most challenging scenarios (B and C). Also, multifrequency RFT allows imaging the metallic cylinder with the nearby crack (scenario C).

When the SNR decreases to +10 dB see Fig. 8, the GPR imaging configuration becomes even less reliable than before and yields acceptable results only in test case C. Conversely, single frequency RFT provides better results, with the exception of case B that is characterized by ambiguous images with many artifacts. Multifrequency RFT provides again superior quality images, which do not suffer from the increased noise

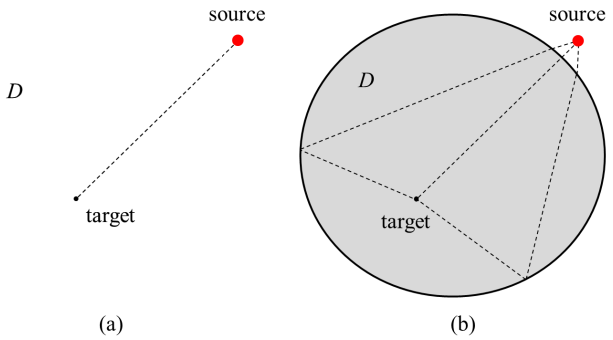

Fig. 6: Simplified representation of the scattering phenomenon. In a homogeneous medium model (a), there is a single ray path from the source to the target. When the medium is modeled as inhomogeneous (b), the target is illuminated by the direct ray and rays undergoing reflections in the pillar,thus increasing the illumination diversity of source.

TABLE III: Entropy of the tomographic images for each test case and SNR value

SNR [dB]	Config.	Scen. A	Scen. B	Scen. C
−10	1	6.64	6.68	6.66
	2	6.60	6.60	6.55
	3	6.24	6.42	5.72
10	1	6.56	6.59	6.25
	2	6.13	6.14	5.02
	3	5.42	5.95	4.95
30	1	6.47	6.56	5.77
	2	6.13	6.16	5.43
	3	5.37	5.93	4.88

level.

The tomographic reconstructions achieved from very noisy data (SNR = -10 dB) are displayed in Fig. 9 and reveal the importance of multifrequency RFT to achieve images with physical meaning in all the considered cases. Indeed, both GPR and single frequency RFT provide completely unreliable results.

Finally, the entropy data of the tomographic images found in each test case are summarized in Tab. III. The observed trend in the data versus SNR and measurement configuration is in full agreement with the previous findings.

V. CONCLUSIONS

We compared different imaging strategies for the non-invasive characterization of pillars. Conventional ground penetrating radar has been compared to single frequency and multifrequency radio frequency tomography. The resolving power of the three configurations has been investigated in detail. Specifically, a Singular Value Decomposition of the relevant scattering operator has revealed that, as a direct consequence of multiscattering effects arising in the pillar, all configurations share a similar spectral coverage and resolution limits. However, the capability to detect a target is strongly dependent on the scenario and the noise level on the data. In this respect, despite the major complexity of the measurement system, multifrequency radiofrequency tomographic configuration has proved to be the most robust and reliable imaging strategy.

The experimental validation of the radio-frequency tomographic approach in the case of concrete pillars will be subject of future work.

REFERENCES

[1] J. H. Bungey and M. G. Grantham, *Testing of concrete in structures*. Taylor & Francis, 2006.

[2] WRAL.com, "Lowe's walkway collapse raises concerns about pedestrian bridge safety, inspections," http://www.wral.com/news/local/story/141306/, updated: 05-21-2000.

[3] J. Hoła and K. Schabowicz, "State-of-the-art non-destructive methods for diagnostic testing of building structures–anticipated development trends," *Archives of Civil and Mechanical Engineering*, vol. 10, no. 3, pp. 5–18, 2010.

[4] D. Breysse, "Nondestructive evaluation of concrete strength: An historical review and a new perspective by combining ndt methods," *Construction and Building Materials*, vol. 33, pp. 139–163, 2012.

[5] K. Karhunen, A. Seppänen, A. Lehikoinen, P. J. Monteiro, and J. P. Kaipio, "Electrical resistance tomography imaging of concrete," *Cement and Concrete Research*, vol. 40, no. 1, pp. 137–145, 2010.

[6] A. Loperte, F. Soldovieri, and V. Lapenna, "Monte cotugno dam monitoring by the electrical resistivity tomography," *IEEE Journal of Selected Topics in Applied Earth Observations and Remote Sensing*, vol. 8, pp. 5346–5351, 2015.

[7] R. Persico, *Introduction to ground penetrating radar: inverse scattering and data processing*. John Wiley & Sons, 2014.

[8] J. Hugenschmidt, "Concrete bridge inspection with a mobile gpr system," *Construction and building materials*, vol. 16, no. 3, pp. 147–154, 2002.

[9] M. Bavusi, F. Soldovieri, R. Di Napoli, A. Loperte, A. Di Cesare, F. C. Ponzo, and V. Lapenna, "Ground penetrating radar and microwave tomography 3d applications for the deck evaluation of the musmeci bridge in potenza, italy," *Journal of Geophysics and Engineering*, vol. 8, no. 3, p. S33, 2011.

[10] J. Hugenschmidt, A. Kalogeropoulos, F. Soldovieri, and G. Prisco, "Processing strategies for high-resolution gpr concrete inspections," *NDT & E International*, vol. 43, no. 4, pp. 334–342, 2010.

[11] V. Perez-Gracia, F. G. García, and I. R. Abad, "Gpr evaluation of the damage found in the reinforced concrete base of a block of flats: A case study," *NDT & e International*, vol. 41, no. 5, pp. 341–353, 2008.

[12] A. Loperte, F. Soldovieri, A. Palombo, F. Santini, and V. Lapenna, "An integrated geophysical approach for water infiltration detection and characterization at monte cotugno rock-fill dam (southern italy)," *Engineering Geology*, vol. 211, pp. 162–170, 2016.

[13] V. Barrile and R. Pucinotti, "Application of radar technology to reinforced concrete structures: a case study," *NDT & e International*, vol. 38, no. 7, pp. 596–604, 2005.

[14] J. Hugenschmidt and R. Loser, "Detection of chlorides and moisture in concrete structures with ground penetrating radar," *Materials and Structures*, vol. 41, no. 4, pp. 785–792, 2008.

[15] S. J. Radzevicius, B. T. Clark, D. Herbst, and T. T. Webster, "Imaging columns with gpr," in *Ground Penetrating Radar, 2004. GPR 2004. Proceedings of the Tenth International Conference on*, vol. 1. IEEE, 2004, pp. 387–390.

[16] G. Leucci, R. Persico, and F. Soldovieri, "Detection of fractures from gpr data: the case history of the cathedral of otranto," *Journal of Geophysics and Engineering*, vol. 4, no. 4, p. 452, 2007.

[17] S. Santos-Assunçao, V. Perez-Gracia, O. Caselles, J. Clapes, and V. Salinas, "Assessment of complex masonry structures with gpr compared to other non-destructive testing studies," *Remote Sensing*, vol. 6, no. 9, pp. 8220–8237, 2014.

[18] L. Lo Monte, D. Erricolo, F. Soldovieri, and M. C. Wicks, "Radio frequency tomography for tunnel detection," *IEEE Trans. Geosci. Remote Sensing*, vol. 48, no. 3, pp. 1128–1137, Mar 2010.

[19] L. Lo Monte, F. Soldovieri, D. Erricolo, and M. C. Wicks, "Imaging below irregular terrain using rf tomography," *IEEE Trans. Geosci. Remote Sensing*, vol. 50, no. 9, pp. 3364–3373, Sep 2012.

[20] V. Picco, T. Negishi, S. Nishikata, D. Spitzer, and D. Erricolo, "RF Tomography in Free Space: Experimental Validation of the Forward Model and an Inversion Algorithm Based on the Algebraic Reconstruction Technique," *International Journal of Antennas and Propagation*, vol. 2013, article ID 528347, doi:10.1155/2013/528347.

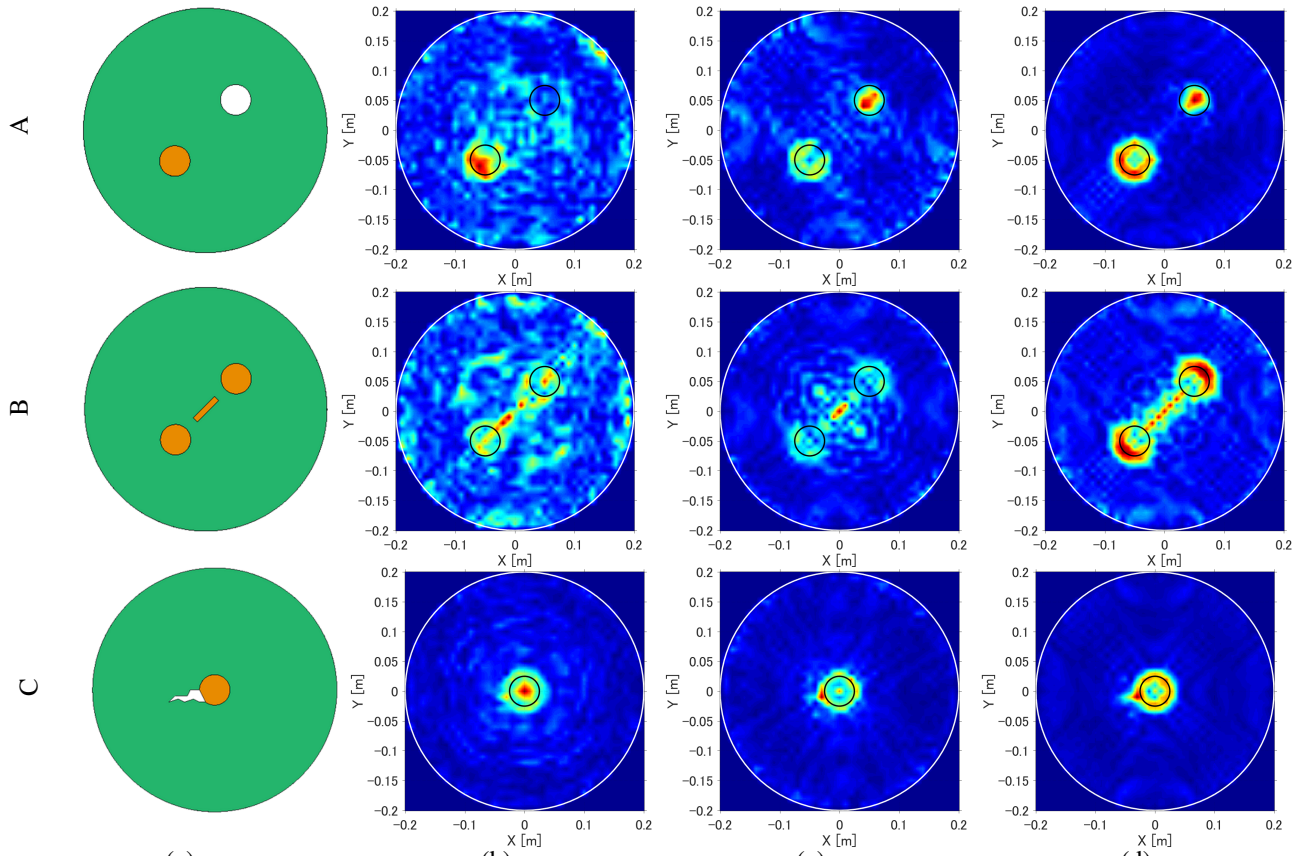

Fig. 7: Tomographic reconstructions achieved from full-wave synthetic data when SNR = +30 dB. (a) Geometry of the scenarios; (b) GPR configuration; (c) Single frequency RFT; (c) Multifrequency RFT. The color scale represents values in the range [0, 1].

[21] V. Picco, G. Gennarelli, T. Negishi, F. Soldovieri, and D. Erricolo, "Experimental validation of the quadratic forward model for rf tomography," *GRSL*, vol. 12, no. 7, p. 1461 – 1465, March 2015.

[22] T. Negishi, G. Gennarelli, F. Soldovieri, and D. Erricolo, "Radio frequency tomography for the investigation of cracks in reinforced concrete structures," in *European Geosciences Union General Assembly*, Vienna, Austria, April 2016.

[23] T. Negishi, V. Picco, D. Erricolo, G. Gennarelli, F. Soldovieri, and P. L. Uslenghi, "Experimental validation of radio frequency tomography for an inhomogeneous medium," in *URSI Commission B International Symposium on Electromagnetic Theory*, Espoo, Finland, August 2016, pp. 5–8.

[24] R. Persico, G. Gennarelli, and F. Soldovieri, "Gpr prospecting on circular surfaces: preliminary results," in *Proceedings of the 15th International Conference on Ground Penetrating Radar*, June 2014, pp. 79–82.

[25] G. Leone, R. Persico, and R. Pierri, "Inverse scattering under the distorted born approximation for cylindrical geometries," *Journal of the Optical Society of America A*, vol. 16, no. 7, pp. 1779–1787, 1999.

[26] W. Chew and Y. Wang, "Reconstruction of two-dimensional permittivity distribution using the distorted born iterative method," *Medical Imaging, IEEE Transactions on*, vol. 9, no. 2, pp. 218–225, 1990.

[27] W. C. Chew, *Waves and fields in inhomogeneous media*. IEEE press, 1995.

[28] M. Bertero and P. Boccacci, *Introduction to inverse problems in imaging*. CRC press, 1998.

[29] R. Solimene, I. Catapano, G. Gennarelli, A. Cuccaro, A. Dell'Aversano, and F. Soldovieri, "Sar imaging algorithms and some unconventional applications: A unified mathematical overview," *IEEE Signal Processing Magazine*, vol. 31, no. 4, pp. 90–98, 2014.

[30] C. Balanis, *Advanced Engineering Electromagnetics*, ser. CourseSmart Series. Wiley, 2012. [Online]. Available: http://books.google.com/books?id=cRkTuQAACAAJ

[31] G. Gennarelli and F. Soldovieri, "Performance analysis of incoherent rf tomography using wireless sensor networks," *IEEE Transactions on Geoscience and Remote Sensing*, vol. 54, no. 5, pp. 2722–2732, May 2016.

[32] P. C. Hansen, "Analysis of discrete ill-posed problems by means of the l-curve," *SIAM review*, vol. 34, no. 4, pp. 561–580, 1992.

[33] P. C. Hansen and D. P. O'Leary, "The use of the l-curve in the regularization of discrete ill-posed problems," *SIAM Journal on Scientific Computing*, vol. 14, no. 6, pp. 1487–1503, 1993.

[34] R. Persico, R. Bernini, and F. Soldovieri, "The role of the measurement configuration in inverse scattering from buried objects under the born approximation," *IEEE Transactions on Antennas and Propagation*, vol. 53, no. 6, pp. 1875–1887, 2005.

[35] G. Gennarelli and F. Soldovieri, "The effect of array configuration in transmission-mode electromagnetic imaging," *IEEE Transactions on Antennas and Propagation*, vol. 62, no. 10, pp. 5148–5156, 2014.

[36] G. Gennarelli, R. Persico, and F. Soldovieri, "Effective imaging systems based on periodic lattices," *Applied Physics Letters*, vol. 104, no. 19, p. 194103, 2014.

[37] G. Gennarelli and F. Soldovieri, "Radar imaging through cinderblock walls: Achievable performance by a model-corrected linear inverse scattering approach," *IEEE Transactions on Geoscience and Remote Sensing*, vol. 52, no. 10, pp. 6738–6749, 2014.

[38] G. Gennarelli, I. Catapano, F. Soldovieri, and R. Persico, "On the Achievable Imaging Performance in Full 3-D Linear Inverse Scattering," *IEEE Trans. Antennas Propag.*, vol. 63, no. 3, pp. 1150–1155, March 2015.

[39] D. Erricolo, "Acceleration of the convergence of series containing mathieu functions using shanks transformation," *IEEE Antennas and Wireless Propagation Letters*, vol. 2, no. 1, pp. 58–61, 2003.

[40] A. Devaney, "Geophysical diffraction tomography," *IEEE Transactions on Geoscience and Remote Sensing*, no. 1, pp. 3–13, 1984.

[41] A. C. Kak and M. Slaney, *Principles of computerized tomographic imaging*. IEEE press, 1988.

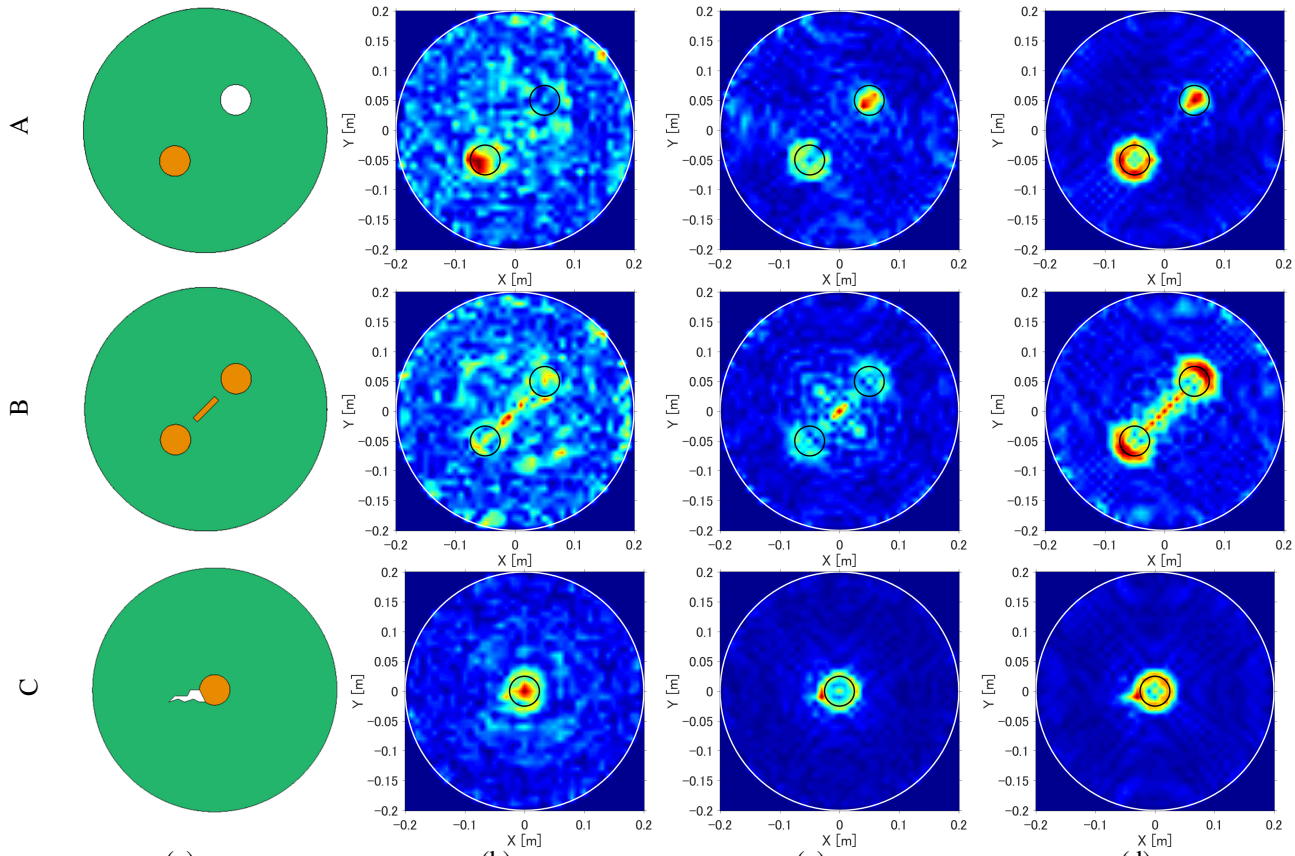

Fig. 8: Tomographic reconstructions achieved from full-wave synthetic data when SNR = +10 dB. (a) Geometry of the scenarios; (b) GPR configuration; (c) Single frequency RFT; (c) Multifrequency RFT. The color scale represents values in the range [0, 1].

[42] G. Gennarelli and F. Soldovieri, "A linear inverse scattering algorithm for radar imaging in multipath environments," *IEEE Geoscience and Remote Sensing Letters*, vol. 10, no. 5, pp. 1085–1089, 2013.

[43] P. Setlur, T. Negishi, N. Devroye, and D. Erricolo, "Multipath exploitation in non-los urban synthetic aperture radar," *IEEE Journal of Selected Topics in Signal Processing*, vol. 8, no. 1, pp. 137–152, 2014.

[44] Altair Engineering, Inc., "FEKO - EM Simulation Software," https://www.feko.info/, updated: 01-11-2011.

[45] R. F. Harrington, *Field computation by moment methods*. Wiley-IEEE Press, 1993.

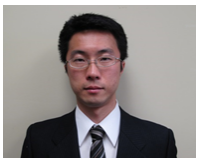

Tadahiro Negishi received the M.S. degree and the Ph.D in Electrical and Computer Engineering from the University of Illinois at Chicago, Chicago, IL, USA, in 2011 and 2018 respectively. Since 2018, he has been working as a Research and Development Engineer at ANSYS Inc. He has co-authored over 50 international peer-reviewed journals and international conferences. His research interests include forward scattering problems such as analytical solutions, computational electromagnetic methods, high frequency techniques, and inverse scattering problems such as RF Tomography and Range Doppler imaging techniques.

Gianluca Gennarelli received the M.Sc. degree (summa cum laude) in electronic engineering and the Ph.D. in information engineering from the University of Salerno, Salerno, Italy, in 2006 and 2010, respectively. From 2010 to 2011, he was a Post-Doctoral fellow at the University of Salerno. Since 2012, he has been a Research Scientist with IREA-CNR, Naples, Italy. In 2015, he was a Visiting Scientist with the NATO-CMRE, La Spezia, Italy. He has co-authored over hundred publications in international peer-reviewed journals and conference proceedings. His research interests include microwave sensors, antennas, inverse scattering problems, radar imaging, diffraction problems and electromagnetic simulation.

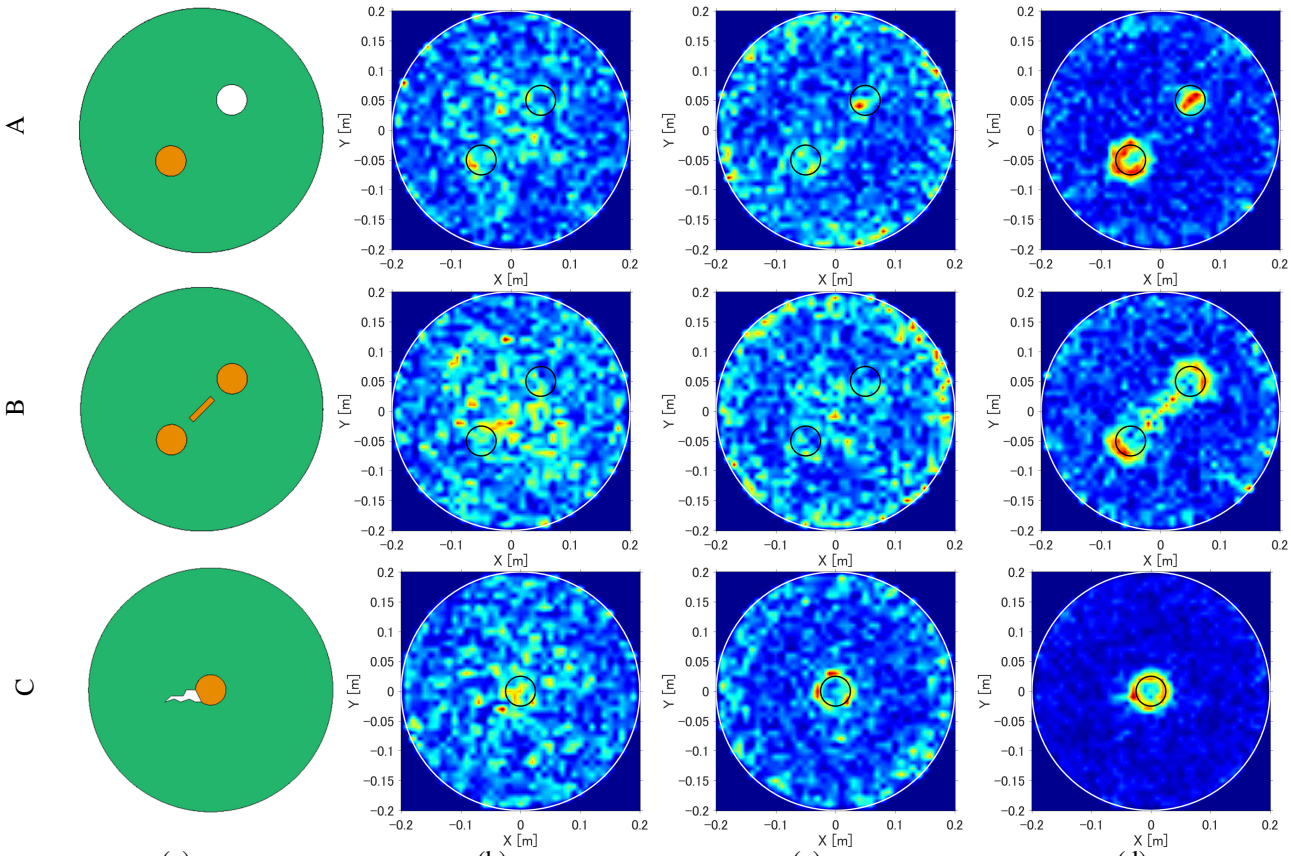

Fig. 9: Tomographic reconstructions achieved from full-wave synthetic data when SNR = -10 dB. (a) Geometry of the scenarios; (b) GPR configuration; (c) Single frequency RFT; (c) Multifrequency RFT. The color scale represents values in the range [0, 1].

Francesco Soldovieri is a Research Director at Institute for Electromagnetic Sensing of the Environment of CNR. He was the General Chair of the International Workshop on Advanced Ground Penetrating Radar 2007 and the General Co-Chair of the Ground Penetrating Radar Conference 2010. He was member of the Editorial Board of IEEE-GRSL and now of IEEE-TCI and IEEE-TGRS, Remote Sensing (MDPI). He is Editor in Chief of HERITAGE, a MDPI journal devoted to Cultural and Natural Heritage. He has been the Scientific Coordinator of the FP7 projects ISTIMES and AMISS and the Technical manager of the H2020 Project HERACLES. He has been the President of the Division on Geosciences Instrumentation and Data Systems of European Geosciences Union. His research interests include radar imaging, data processing for GPR, indoor surveillance, through-wall imaging, passive radars, integration of geophysical data, radars for planetary exploration. He is the co-author of about 240 papers on national and international Journals and more than 350 conference proceedings.

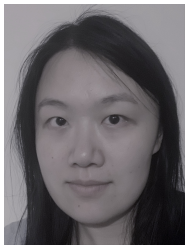

Yangqing Liu Yangqing Liu is currently a PhD student in the Andrew Electromagnetics Laboratory at the University of Illinois at Chicago.

Danilo Erricolo (S'97-M'99-SM'03-F'16) received the Laurea degree of Doctor (summa cum laude) in electronics engineering from the Politecnico di Milano, Milan, Italy, in 1993 and the Ph.D. degree in electrical engineering and computer science from the University of Illinois at Chicago (UIC), Chicago, IL, USA, in 1998. He is a Professor in the Department of Electrical and Computer Engineering, the Director of the Andrew Electromagnetics Laboratory, and an adjunct Professor of Bioengineering at UIC. In 2017 he was nominated a University of Illinois Scholar. During the summer of 2009, he was an Air Force Faculty Fellow at the Air Force Research Laboratory, Wright-Patterson Air Force Base in Dayton, OH, USA. He has authored or coauthored more than 270 publications in refereed journals and international conferences. He has served as Associate Editor of the IEEE ANTENNAS AND WIRELESS PROPAGATION LETTERS (2002-2014), the IEEE TRANSACTIONS ON ANTENNAS AND PROPAGATION (2013-2016) and of Radio Science (2014-2016). In 2006, he was the Guest Editor of the special issues on RF effects on digital systems of the Electromagnetics Journal, and in 2012 he was the Lead Guest Editor of the special issue on Propagation models and inversion approaches for subsurface and through wall imaging, of the International Journal of Antennas and Propagation. His research interests are primarily in the areas of antenna design, electromagnetic propagation and scattering, high-frequency techniques, wireless communications, electromagnetic compatibility, the computation of special functions, and magnetic resonance imaging. Dr. Erricolo was elected Full Member of Commissions B, C and E of the U.S. National Committee (USNC) of the International Union of Radio Science (URSI), a committee of the US National Academies. He served as Chair (2009-2011), Vice Chair (2006-2008) and Secretary (2004-2005) of the USNC-URSI Commission E on Electromagnetic Environment and Interference. He was Chair of the USNC-URSI Ernest K. Smith Student Paper Competition (2009-2014); Vice-Chair of the Local Organizing Committee of the XXIX URSI General Assembly, held in Chicago, IL, USA in August 2008; and Member at Large of USNC-URSI (2012-2017). He served on the IEEE Antennas and Propagation Society (AP-S) Future Symposia Committee and on the IEEE AP-S/USNC-URSI Joint Meetings Committee (2006-2017 as a USNC-URSI representative). He was the General Chairman of the 2012 IEEE International Symposium on Antennas and Propagation and USNC-URSI National Radio Science Meeting, held in Chicago, IL, USA in July 2012. He was an Elected Member of the IEEE AP-S Administrative Committee (2012-2014); Chair of the IEEE AP-S Distinguished Lecturer Program (2015-2016); and Chair of the Chicago Joint Chapter of the IEEE AP-S and Microwave Theory and Techniques Society (2011-2016). He has served on more than 40 conference technical program committees, chaired over 60 conference sessions and organized more than 20 special sessions at international scientific conferences. He has been the Editor-in-Chief of the IEEE TRANSACTIONS ON ANTENNAS AND PROPAGATION since August 2016.